An Energy Localization Principle and its Application to Fast Kinetic Monte Carlo Simulation of Heteroepitaxial Growth

Tim P. Schulze
Department of Mathematics
University of Tennessee, Knoxville, TN 37909-1300

and

Peter Smereka
Department of Mathematics and
Michigan Center for Theoretical Physics
University of Michigan, Ann Arbor, MI 48109-1109

Abstract

Simulation of heteroepitaxial growth using kinetic Monte Carlo (KMC) is often based on rates determined by differences in elastic energy between two configurations. This is computationally challenging due to the long range nature of elastic interactions. A new method is introduced in which the elastic field is updated using a local approximation technique. This involves an iterative method that is applied in a sequence of nested domains until a convergence criteria is satisfied. These localized calculations yield energy differences that are highly accurate despite the fact that the energies themselves are far less accurate: an effect referred to as the principle of energy localization. This is explained using the continuum analogue of the discrete model and error estimates are found. In addition, a rejection algorithm that relies on a computationally inexpensive estimate of hopping rates is used to avoid a substantial fraction of the elastic updates. These techniques are applied to $1+1$ dimensional KMC simulations in physically interesting regimes.

1   Introduction

Heteroepitaxial growth consists of slowly depositing one material onto a crystalline substrate formed from a second material. A classic example is Germanium deposited onto a Silicon substrate. An important feature of this

process is that the natural lattice spacing of the deposited material can be different from the substrate's, resulting in elastic strain. The total elastic energy stored in the film is reduced when three dimensional islands form, making this the preferred morphology despite an increase in surface energy. In many cases the three dimensional islands that arise are as small as tens of nanometers in size and are referred to as *quantum dots* [24, 31], due to their unique electronic properties. For example, solid state lasers have been made out of such materials. In addition, there is hope that such materials may be useful in quantum computing applications.

Heteroepitaxy has often been studied using fully continuum models, where the formation of quantum dots (islands) is known as the Asaro-Tiller-Grinfeld instability [1, 13]. The morphological instability leading to island formation has been studied extensively [35, 9, 32, 33, 7]; see Gao [10] for a more extensive review. More recent works adopting the continuum approach include [34, 36, 37, 39, 40] .

In this work, we adopt an alternative, atomistic approach developed by Orr *et al.* [23], Lam, Lee and Sander (LLS) [15], and Lung *et al.* [20]. Elastic interactions are accounted for using a ball and spring model, chemical interactions with a solid-on-solid (*i.e.*, no voids or overhangs) bond-counting model, and the system is evolved in time using kinetic Monte Carlo (KMC). While this model is idealized, it nevertheless captures the essential physical effects of heteroepitaxial growth, such as adatom diffusion, nucleation, surface diffusion, and long range elastic interaction. In addition, KMC naturally captures effects associated with fluctuations and noise. Related work includes models of heteroepitaxy using the Frenkel-Kontorova model [25, 26] and off-lattice KMC simulations [2, 12, 21, 22].

In order to implement a standard rejection-free KMC method one must tabulate a list of all the rates and then choose an event at random with a probability proportional to its rate. Therefore to move an atom we must know the hopping rate of all the atoms. For heteroepitaxy, this would entail computing the change in elastic energy for each possible move. To overcome this computational bottleneck, we combine inexpensive, relatively sharp, upper bounds on the individual rates with rejection. This allows us to avoid pre-computing the rates for all possible moves for a given system configuration. Instead, a single atom is selected using the approximate rates and a decision of whether or not to move that atom is then based on a single subsequent elastic computation.

Since the displacement field is very nonlocal and at least two calculations

2

must be made for each accepted move—once with the atom removed and, when a move is accepted, once in its final location—this is still prohibitive. The Fourier-multigrid algorithm developed in [29] helps with this (see also Ref. [4]), but we find we can do better using approximate local calculations centered on the locations of the atom being moved. Whenever an atom is added or removed from the lattice, we implement an efficient iterative technique based on successive over-relaxation to update the displacement field in a sequence of nested domains until a convergence criteria is satisfied. This exploits the fact that changes to the system's configuration naturally propagate outward from the moving atom.

One might expect this approach to be rather poor, owing to the long range of elastic interactions. To explain why this is not the case, in §5 we shall use the theory of continuum elasticity, combined with a small slope approximation, to study a film with a stress-free strain on top of a semi-infinite substrate. We compute the difference in the elastic energy density between the original film and one where a localized amount of material has been removed. It is established that this quantity decays, but *very slowly*. One might view this as a Saint-Venant's Principle [30] (see, for example, [18] or [38]) for the density of the elastic energy change. Despite this slow decay, we are able to prove, for the specific geometry of an island sitting on a wetting layer which, in turn, is on a substrate, that the numerical approach described above will in fact provide accurate estimates for the change in elastic energy when an atom is removed. This implies that our approach is able to localize the energy change while at the same time providing an accurate displacement field.

Finally, we remark that one could develop similar theorems for the case in which a stressed film is sandwiched between two semi-infinite "substrates" and material is removed from the stressed film. For an arbitrarily shaped, but finite, removed region, it appears that our results can be extended using the mean value theorems of Diaz and Payne [5] (a discussion can also be found in [14]) without resorting to the small slope approximation.

2   Model Description

We now describe the LLS model [15]. This is a solid-on-solid model in which the height of the film at lattice location i is given by the integer h_i where $i = 1, 2, 3, ..., M$. The hopping rate associated with the ith surface atom is

3

r_i. When an atom hops it moves k steps from its current location, where k is a random variable uniformly distributed on $\{\pm 1, \pm 2, ..., \pm K\}$. The hopping rate is modeled as

$$r_i = r_0 \exp\left[\left(-\gamma n + \Delta W + E\right)/k_B T\right], \tag{1}$$

where n is the total number of nearest neighbor and next nearest neighbor (diagonal) bonds, γ is the bond energy, $k_B T$ is the thermal energy, and r_0 is given by

$$r_0 = \frac{12D}{(K+1)(2K+1)}. \tag{2}$$

The constants E and D are chosen so that adatom diffusion will match experimental values. The expression given by (2) ensures that the diffusion rate on a flat surface will be independent of K. The elastic correction to the energy barrier is given by ΔW, which is modeled as

$$\Delta W = W(\text{with atom } i) - W(\text{without atom } i),$$

where W is the total elastic energy. Deposition is incorporated by adding atoms at a rate

$$r_{dep} = (K+1)(2K+1)F/6,$$

where F is the deposition rate in monolayers per unit time. It was shown in LLS[15] that the dynamics is relatively insensitive to the choice of K. However, the computational speed can be greatly increased with larger choices of K.

Apart from the ΔW term, the hopping rate r_i can be easily calculated by bond counting. The ΔW term, on the other hand, requires considerably more effort. First, one must calculate the equilibrium displacement field and evaluate the total elastic energy. Second, one must remove the ith atom, recalculate the displacement field, compute the total energy, and then take the difference.

We now describe the discrete elastic model. It is useful to introduce the misfit

$$\mu = \frac{a_g - a_s}{a_s}, \tag{3}$$

where a_s is the lattice spacing of the substrate atoms and a_g is the lattice spacing deposited atoms. Typical values of μ range from -0.05 to 0.05. For example, the misfit for Germanium on a Silicon substrate is 0.04.

In this elastic model, neighboring atoms are connected with springs—nearest neighbors having spring constant k_L and next-nearest neighbors having spring constant k_D. We employ a reference configuration that consists of a periodic array of complete layers of, say, Germanium atoms on top of a periodic array of, say, Silicon atoms, with the Germanium atoms compressed so that their horizontal lattice spacing matches that of the Silicon. The vertical lattice spacing, a_L, is chosen so that the resulting system is in mechanical equilibrium. One can show that

$$a_L = a_g + a_s \mu \frac{k_D}{k_L + k_D}. \tag{4}$$

Note that the atoms are always on a rectangular lattice of size $M \times N$ with a solid-on-solid constraint enforced. The atom located at site (i, j) has a displacement field $(u_{i,j}, v_{i,j})$. In addition, we introduce the following variable defined on this lattice

$$p_{i,j} = \begin{cases} 1 & \text{if } (i,j) \text{ contains an atom} \\ 0 & \text{if } (i,j) \text{ otherwise.} \end{cases}$$

We also define

$$\sigma_{i,j;m,n} = p_{i,j} p_{i+m,j+n}. \tag{5}$$

For this model the total elastic energy is

$$W = \frac{1}{2} \sum_{i,j} w_{i,j},$$

where

$$w_{i,j} = w_{i,j}^{xx} + w_{i,j}^{yy} + 2w_{i,j}^{xy}, \tag{6}$$

and

$$
\begin{aligned}
w_{ij}^{xx} &= \frac{k_L}{2} \left(\sigma_{i,j;1,0}(u_{i+1,j} - u_{i,j} - d_1)^2 + \sigma_{i,j;-1,0}(u_{i-1,j} - u_{i,j} + d_1)^2 \right) \\
&+ \frac{k_D}{4} \left(\sigma_{i,j;1,1}(u_{i+1,j+1} - u_{i,j} - d_1)^2 + \sigma_{i,j;-1,-1}(u_{i-1,j-1} - u_{i,j} + d_1)^2 \right. \\
&\left. \qquad + \sigma_{i,j;1,-1}(u_{i+1,j-1} - u_{i,j} - d_1)^2 + \sigma_{i,j;-1,1}(u_{i-1,j+1} - u_{i,j} + d_1)^2 \right), \\
w_{ij}^{yy} &= \frac{k_L}{2} \left(\sigma_{i,j;0,1}(v_{i,j+1} - v_{i,j} - d_2)^2 + \sigma_{i,j;0,-1}(v_{i,j-1} - v_{i,jj} + d_2)^2 \right) \\
&+ \frac{k_D}{4} \left(\sigma_{i,j;1,1}(v_{i+1,j+1} - v_{i,j} - d_2)^2 + \sigma_{i,j;-1,-1}(v_{i-1,j-1} - v_{i,j} + d_2)^2 \right.
\end{aligned}
$$

5

$$+ \sigma_{i,j;1,-1}(v_{i+1,j-1} - v_{i,j} + d_2)^2 + \sigma_{i,j;-1,1}(v_{i-1,j+1} - v_{i,j} - d_2)^2\big) ,$$

$$\begin{aligned}
w_{ij}^{xy} = \frac{k_D}{4} \big(&\sigma_{i,j;-1,-1}(u_{i-1,j-1} - u_{i,j} + d_1) \ (v_{i-1,j-1} - v_{i,j} + d_2) \\
&+ \sigma_{i,j;1,1}(u_{i+1,j+1} - u_{i,j} - d_1)(v_{i+1,j+1} - u_{i,j} - d_2) \\
&- \sigma_{i,j;1,-1}(u_{i+1,j-1} - u_{i,j} - d_1)(v_{i+1,j-1} - v_{i,j} + d_2) \\
&- \sigma_{i,j;-1,1}(u_{i-1,j+1} - u_{i,j} + d_1)(v_{i-1,j+1} - v_{i,j} - d_2) \ \big) ,
\end{aligned}$$

$$d_1 = \begin{cases} a_g - a_s & \text{for g-g and s-s bonds} \\ 0 & \text{for s-s bonds} \end{cases} \tag{7}$$

and

$$d_2 = \begin{cases} a_g - a_L & \text{for g-g and g-s bonds} \\ 0 & \text{for s-s bonds} \end{cases} . \tag{8}$$

The equilibrium configuration is determined from

$$\frac{\partial W}{\partial u_{i,j}} = 0 \quad \text{and} \quad \frac{\partial W}{\partial v_{i,j}} = 0,$$

which results in a linear system of equations

$$AU = F, \tag{9}$$

where U is a vector containing the unknown displacement fields. These equations are presented in [29] (see Eqs. 4 and 5). Also in [29], a method based on a combination of multigrid and discrete Fourier transforms was used to develop an efficient algorithm to solve (9).

We remark that the three dimensional version of Eq. 6 presented in [28] is incorrect: the cross terms were inadvertently not included. The discrete equations for the displacement field are, however, correct.

3   Computational Methods

In this section we explain three improvements over earlier computational work on this model. First, we implement easily computed rate estimates $\hat{r}_i \geq r_i$ that are tailored to the local topography, greatly reducing the number of rejections and, hence, unnecessary applications of the elastic solver. Second, we describe a technique that greatly improves the calculation of the elastic binding energy based on local calculations. Finally, we describe an efficient technique for performing local elastic updates in response to isolated changes in the system configuration.

3.1 Upper Bounds on Rates

In a standard implementation of kinetic Monte Carlo the hopping rate of each surface atom must be known. For the model we have adopted this would entail finding the change in elastic energy for each and every atom just to move one atom. This would then be repeated after each move. Even with the efficient techniques for updating the displacement field outlined above, such an algorithm would be far too slow to be practical. On the other hand, suppose we had a reasonably sharp upper bound for the elastic energy change that was inexpensive to evaluate. In view of (1), one would have an upper bound, $\hat{r}_i$, on the hopping rate. Atoms are now selected with a probability proportional to $\hat{r}_i$. At this point, the change in elastic energy will be calculated and the actual rate will be revealed. The hop is then accepted with a probability $r_i/\hat{r}_i$. If the upper bound is close to the actual rate then the rejection rate will be small. In this way, one gains considerable computational savings by avoiding elastic calculations for moves that will ultimately be rejected.

We have found, based on physical intuition, a reliable approximate upper bound on the change in elastic energy. This is explained by first noting that the total elastic energy can be written as

$$W = \frac{1}{2} \sum_p e_p,$$

where e_p is the elastic energy stored in the springs connected to atom p. If atom p is located at (i,j), $e_p = w_{i,j}$ (see Eq. 6). The factor $1/2$ is the result of double counting of bonds in the sum over atoms. It was found through numerical experiments, in 1+1 dimensions, that

$$\Delta W < \Delta \widehat{W} \equiv C(n)e_p, \quad \text{where} \quad C(n) = \begin{cases} 1.5 & n = 3 \\ 2.4 & n = 4 \\ 3.5 & n \geq 5. \end{cases} \tag{10}$$

This leads to the following upper bound on rates

$$\hat{r}_i = r_0 \exp\left((-\gamma n + \Delta\widehat{W} + E)/k_B T\right). \tag{11}$$

Note that for a low-curvature surface, one can anticipate e_p will be positive based on a general principle that the energy increases (decreases) as mass is

7

added (removed) from the system; see, for example the discussion in [8] on p. 557.

As it turns out in most cases $\Delta \widehat{W}$ is only slightly greater than ΔW. For this reason the rejection rate is typically quite small (.005 to .04). Finally we point out another approach for obtaining upper bounds was used in [15, 20] and the details can be found in [16].

3.2 Energy Localization Method

Despite the reduction in the number of elastic calculations provided by the local rate estimates, the dominant computational task is still the repeated update of the displacement field in response to isolated changes in the system configuration. It is natural to attempt a local correction to the displacement field when a single atom is added or removed, an intuition consistent with Saint-Venant's Principle [30] (see, for example, [18]) regarding the decay of the influence of localized forces.

Suppose we wish to calculate the elastic energy barrier for an atom to hop. Let $\mathbf{u} = (u, v)$ be the exact displacement field and $\mathbf{u}^a$ be the exact displacement with the atom removed. The exact energy barrier for the hop is

$$\Delta W = W(\mathbf{u}) - W(\mathbf{u}^a).$$

The energy localization method is an approximation to this barrier based on a local solution $\mathbf{u}_\rho^a$ with the atom off in a subset $\Omega_\rho^a \subset \Omega$ of the original computational domain having a characteristic size ρ. Importantly, the displacement of the local solution on the boundary is constrained to agree with the atom-on solution $\mathbf{u}$; see Figure 1.

To assess the accuracy of a local solution, the residual, defined as

$$R = AU - F, \tag{12}$$

is computed. We define the global residual error as

$$R_G = ||R||_2 / ||F||_2,$$

where $|| \cdot ||_2$ is the discrete L^2 norm. The local residual error in a region Ω_ρ is defined as

$$R_L = \frac{1}{\mu a_s k_L} \max_{\Omega_\rho} |R| \tag{13}$$

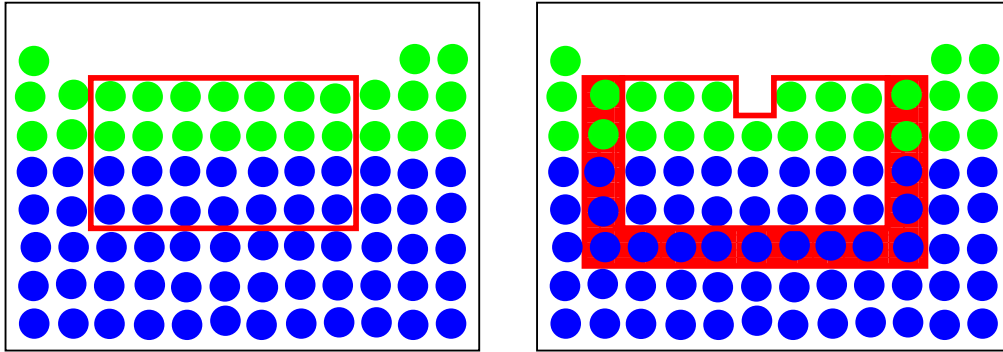where both R_G and R_L are dimensionless.

8

Figure 1: The region Ω_ρ^a is composed of the atoms contained in the red box in the figure on the right. This is the set of points in which the displacement field, $\mathbf{u}_\rho^a$, is updated using the displacements of the atoms in Γ_ρ (surrounded by red) as Dirichlet boundary conditions. The region Ω_ρ is shown in the figure on the left and is used for the local elastic "energy on" calculation, whereas Ω_ρ^a is for the local "energy off" calculation (color available on-line).

A local calculation is considered successful if R_L is sufficiently small, with the residual typically decreasing as the characteristic size ρ of the local region increases. This implies that the atoms just outside the last shell have a small net force and are therefore somewhat out of equilibrium. If the entire system were allowed to relax, this would have a small global effect on the displacement field, but, as we shall see, the cumulative effect on the elastic energy can still be significant.

A local elastic energy barrier is defined to be

$$\Delta W_L = W(\mathbf{u}; \Omega_\rho) - W(\mathbf{u}_\rho^a; \Omega_\rho^a), \tag{14}$$

where $W(\mathbf{u}; \Omega_\rho)$ is the energy associated with a given set of atoms Ω_ρ and Ω_ρ^a is Ω_ρ with one atom removed. The reader is reminded that $\mathbf{u}_\rho^a$ is a local solution where $\mathbf{u}_\rho^a = \mathbf{u}_\rho$ for the atoms on the lower boundary Γ_ρ; see Figure 1.

Numerical computations reveal the following observations.

OBSERVATION 1 - Residual Estimate. *The local residual error, R_L, decreases with the characteristic size, ρ, of the local region.*

OBSERVATION 2 - Energy Barrier Localization. *When R_L is small we find*

$$\Delta W_L \approx \Delta W.$$

An important point is that the residual can be computed inexpensively, whereas an actual calculation of the error in (14) would require a global computation.

Notice that, with a local solution in a region with characteristic size ρ_1, computing (14) in a region Ω_ρ^a any larger than this will have no effect, as the displacement field outside this region is the same for the atom on and off. However, using a smaller region for the energy calculation leads to very poor results. Surprisingly, this is true even if the elastic fields for the atom on and off are the result of full global solutions and we use a region for the energy calculation large enough that a local solution of the displacement field would have been accurate:

$$\Delta W_T = W(\mathbf{u}; \Omega_\rho) - W(\mathbf{u}^a; \Omega_\rho^a). \tag{15}$$

Indeed, such an approximation is quite poor.

OBSERVATION 3 - Energy Nonlocality. *The approximation $\Delta W \approx \Delta W_T$ is poor, even when computed in a relatively large region.*

Later, in §5 we characterize these observations further by proving analogous results in the continuum limit for smooth, small amplitude film profiles. Intuitively, it appears that constraining the outermost shell of atoms traps any change of energy due to removing an atom within the local region, so that one gets a very good approximation to the exact energy barrier. Strictly speaking, our results assume the initial, atom-on, field is exact, but extensive numerical experiments demonstrate that this remains true if we start with fields that are the result of multiple local approximations. It is important, however, that the boundary data be of sufficient quality to reflect the effects of the topography over large length scales. For example, calculations with the correct local configuration and zero displacement boundary conditions for the atom on and off give poor results.

REMARK - Observation 1 is expected, but given Observation 3, Observation 2 is quite unexpected.

3.3   Expanding Box Method

Again noting that the dominant numerical task is repeatedly accounting for *isolated* changes in the system configuration, it is efficient to use a local
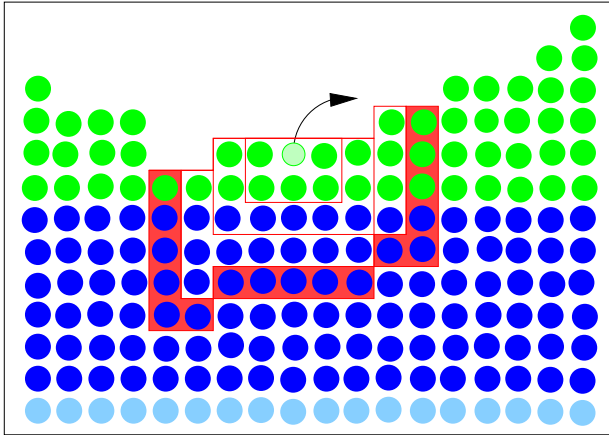
Figure 2: Schematic for the Expanding Region. The hop is indicated with the arrow. Three iterations of the expanding region method have been applied. The atoms surrounded by red are used as Dirichlet conditions on the last of these. When a full elastic computation is peformed, the displacement field of the dark blue and the green atoms are updated using the Fourier-multigrid method in [29] (the displacement of the light blue atoms is deduced using an artificial boundary condition [28].)

solution technique that exploits the fact that any changes in the displacement field will propagate outward from the location of this isolated change.

We adopt a simple iterative technique with successive over-relaxation. Since we are starting from a system which is, to a certain level of accuracy, relaxed, the first iteration of the displacement field will have negligible effect for lattice points that are more than one lattice spacing from the change. Similarly, the second iteration will have significant impact up to two lattice spacings from the site of the change. In this way, the effect of any localized change continues to propagate into the lattice at the rate of one site per iteration. For this reason, we apply SOR (method of successive over relaxtion) on a region that expands no faster than this, as illustrated in Figure 2. In view of the energy localization observations, the boundary values for the displacement field are taken to be pre-correction values. Extensive experimentation with this technique indicates two applications of SOR for each box size is optimal for typical calculations. Iterating more than this is often wasteful as the box is going expand further.

In cases where the size of the expanding box exceeds a threshold S, we abandon the local calculation in favor of a global one. If the threshold is set too small, the solution reverts to a global calculation too frequently; if it is set too large, then a local update can take longer than an application

of the Fourier-multigrid method. For our calculations we found the optimal value was around 50 lattice spacings, but this ultimately is a function of the error tolerance. Typically, global solutions were needed for especially difficult configurations or as the result of accumulating errors in the displacement field after many local updates.

3.4   The Algorithm

We now present an algorithm based on the ideas outlined in sections 3.1 to 3.3. First, we briefly review how to calculate a global update of the displacement field which uses a solution of the discrete half-plane problem by fast Fourier Transforms [28, 19]. In effect, this provides an artificial boundary condition by mapping displacements to forces. In principle, this boundary condition could be applied to any layer of the substrate and in previous work was typically placed at the interface between substrate and film. However, to implement the expanding box method, we need to update the displacement field in a neighborhood of a moving atom. This requires us to place the artificial boundary condition at a depth greater than or equal to the maximum allowable size S of the expanding box. Therefore, as shown in Figure 2, we place the artificial boundary condition, indicated with light blue, at depth S below the substrate. The displacements of all remaining atoms, including substrate atoms, colored blue, and film atoms, colored green, must be computed by other means. The algorithm described below assumes that all of these remaining displacements have been initialized by what we refer to as a full elastic solution. This is computed by the Fourier multi-grid method of Russo & Smereka[29]. The algorithm then proceeds as follows:

1. Select an event by choosing a uniformly distributed random number $r \in [0, \hat{R})$, with $\hat{R} = r_{dep} + \sum \hat{r}_i$. This interval represents an overestimate of the sum of rates for atoms hopping plus the rate of deposition. The event to which r corresponds is located using a binary tree search [3].

2. If the event is a deposition, locally update the height & connection arrays and attempt a local elastic solution; revert to a full elastic computation if the expanding box exceeds size S. Update the rate estimates using (11) in the same region in which the elastic field was updated. Return to Step 1.

3. If the event selected is a hop, then take into account elastic effects:

12

(a) Make a copy of the displacement field $\mathbf{u}_\rho$ (atom on). Follow the same procedures in Step 2 to compute the displacement field with the atom removed, $\mathbf{u}_\rho^a$ (atom off).

(b) Once the elastic field has been updated (locally or globally as necessary), calculate the energy barrier and actual rate r_i $(\leq \hat{r}_i)$.

(c) Use rejection to decide whether or not to make the move. Note that the atom-off calculation must be performed whether or not this move is made.

(d) If the move is rejected, no change is made to the displacement field. Return to Step 1.

(e) If the move is accepted, a hop is made. Update the displacement field in the vacated position using $\mathbf{u}_\rho^a$. Perform a second local/global calculation in the atom's new position thereby updating $\mathbf{u}$.

4. Return to Step 1. One event has been completed.

4 Results

In this section we present an important test case, a comparison with a result from LLS [15], and some new results. We shall use the same parameters, which were chosen to model the growth of Germanium on Silicon. For the convenience of the reader we recall the formula for the hopping rate

$$r_i = r_0 \exp\left[\left(-\gamma N + \Delta W + E\right)/k_B T\right],$$

with

$$r_0 = 12D/((K+1)(2K+1)).$$

Following LLS [15], we take

$$D = D_0/a_s^2 \quad \text{and} \quad K = 8,$$

where $a_s = 2.715$ Å (the lattice spacing of Silicon), $D_0 = 3.83 \times 10^{13}$ Å^2/sec, $E = 0.53$ eV, and $\gamma = 0.4$ eV. For this choice, adatom diffusion will match experimental values. The spring constants are taken to be $k_L = 13.85$ eV/a_s^2 and $k_D = k_L/2$. In this way, the model matches the bulk and shear modulus of Silicon.

4.1 Test Case

One test of our algorithm proceeds as follows. First, consider a typical film profile (e.g. Figure 3a) and compute the displacement field, $\mathbf{u}$, using the Fourier-Multigrid method (a global computation). Second, remove an atom and update the displacement field with the Fourier-Multigrid method, denoting this as $\mathbf{u}^a$. The change in elastic energy is $\Delta W = W(\mathbf{u}) - W(\mathbf{u}^a)$, and we shall refer to this as the exact value for the change in elastic energy. Next, put the atom back and replace the displacement field by $\mathbf{u}$. Repeat this procedure for every surface atom.

Now, we want to compare this to a computation of the displacement field for the atom-off configuration using the expanding box method instead of using the Fourier-multigrid method. This displacement field is denoted as $\mathbf{u}_\rho^a$. One then calculates the change in elastic energy using the approach outlined in §3. In this way, we have $\Delta W_L = W(\mathbf{u}, \Omega_\rho) - W(\mathbf{u}_\rho^a, \Omega_\rho^a)$. Numerical experiments reveal that ΔW is well approximated by ΔW_L provided that ρ is chosen large enough so that the local residual is small. Typically we choose a tolerance of 10^{-2} so that $R_L < 10^{-2}$ (R_L is given by Eq. 13).

While this is a reasonable test, it is lacking one important feature. Namely, in virtually all circumstances, the displacement field, $\mathbf{u}$, will *not* be the result of a global update using the Fourier-Multigrid method, instead it will be a displacement field that has been updated many times using the expanding box method. We shall refer to this displacement field as the approximate atom-on field, $\mathbf{u}_{app}$. Now we apply the expanding box method to compute the change in elastic energy using $\mathbf{u}_{app}$ instead of $\mathbf{u}$. To mimic an approximate atom-on field we first compute the global elastic field corresponding to a perturbed interface where every 20th atom has been removed and midway between removed atoms an atom has been added. Next, we restore the film back to its original profile one atom at a time while updating the displacement field locally using the expanding box method. Now we perform the test described above but using $\mathbf{u}_{app}$ instead of $\mathbf{u}$.

The top of Figure 3 shows a subsection of the profile we used for the test. The middle figure shows a plot of the exact energy change, ΔW (in blue, mostly obscured), the approximate energy change using the expanding box method ΔW_L (in red), and the naive approximation ΔW_T (in green, using a generous $\rho = 50$) all as a function of atom location. The bottom figure shows the size of the expanding box, ρ, that was needed to achieve $R_L < 10^{-2}$. As one can see the expanding box method provides a very
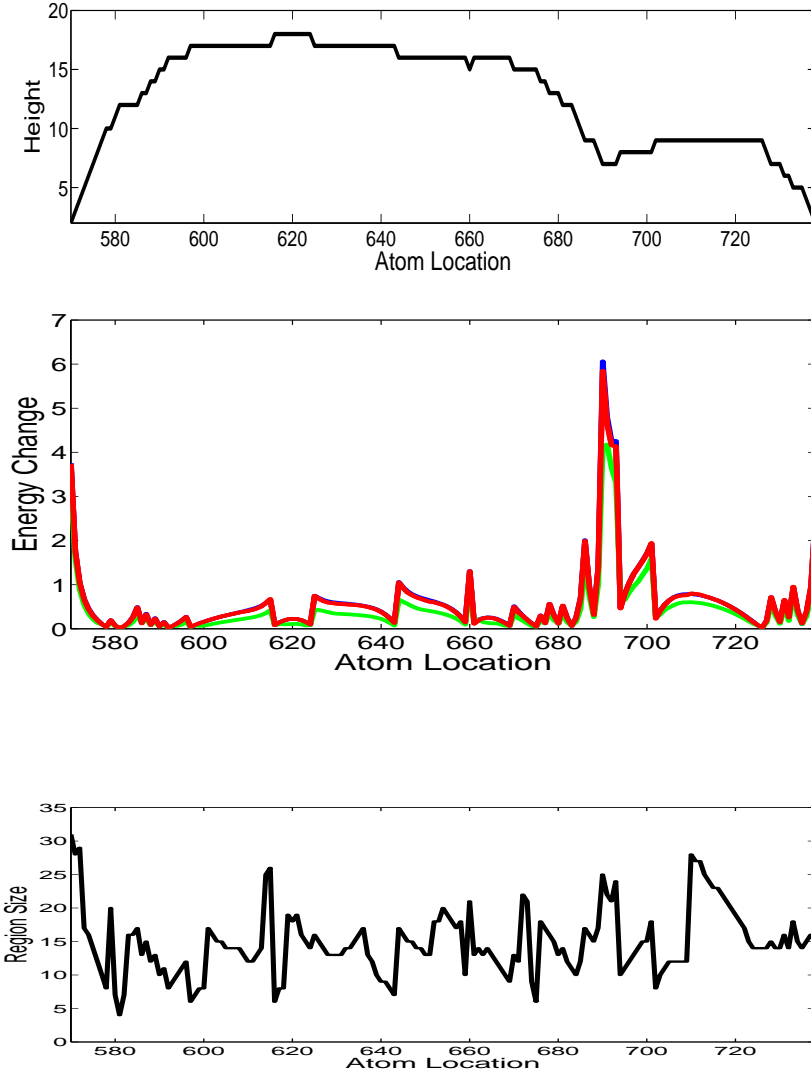
Figure 3: The top curve shows the film height. The middle figure shows the calculation of the change in elastic energy using a full elastic computation (the blue curve, largely hidden). The green curve displays the change in elastic energy for a region with $\rho = 50$. The red curve shows the result using the expanding box method. The last figure shows the size of the region used when obtaining the red curve. In these simulations $R_L < 10^{-2}$.
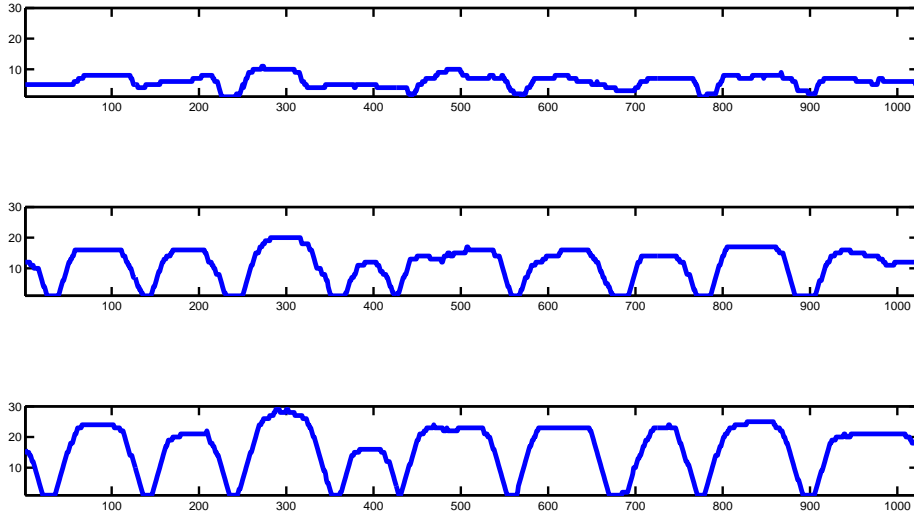
15

Figure 4: Evolution of film growth with $F = 0.8$ monolayers/second, $T = 600$ K, $R_G < 10^{-2}$ and $R_L < 10^{-2}$. The total number of events was 1.09×10^7. There were a total of 223 global elastic computations. The rejection rate was initially 0.0009 and increased to 0.032. The total computation time was two hours on a 2.6 GHz dual core linux box.

accurate approximation. In particular note that in many cases, the size of the expanding box is much less than 50 which was the fixed valued used for ΔW_T.

4.2   Growing Films

We now compare our results to Figure 2c of Ref [15]. This means we will use $\mu = 0.04$, $F = 0.8$ monolayers/sec, and $T = 600$ K. For the results shown in Figure 4 we used the following tolerances on the residuals: $R_G < 10^{-2}$ and $R_L < 10^{-2}$. The results obtained are in good agreement with those found by LLS [15]. Figure 5 shows the same calculation except that $R_G < 10^{-3}$ and $R_L < 10^{-3}$. These are similar to the previous case suggesting that the lower
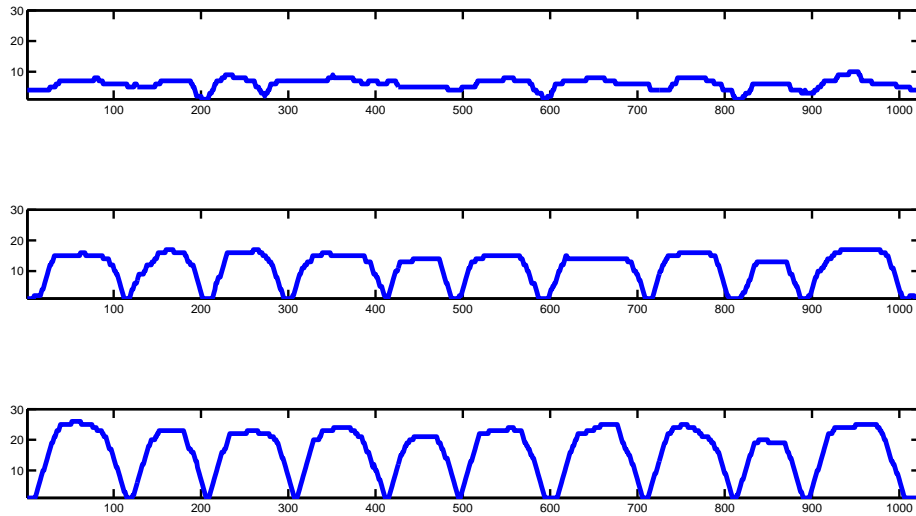
Figure 5: Evolution of film growth with $F = 0.8$ monolayers/second, $T = 600$ K, $R_G < 10^{-3}$ and $R_L < 10^{-3}$. The total number of events was approximately 1.1×10^7. There were a total of 234,194 global elastic computations. The rejection rate was initially 0.0009 and increased to 0.044 The total computation time was 30 hours.
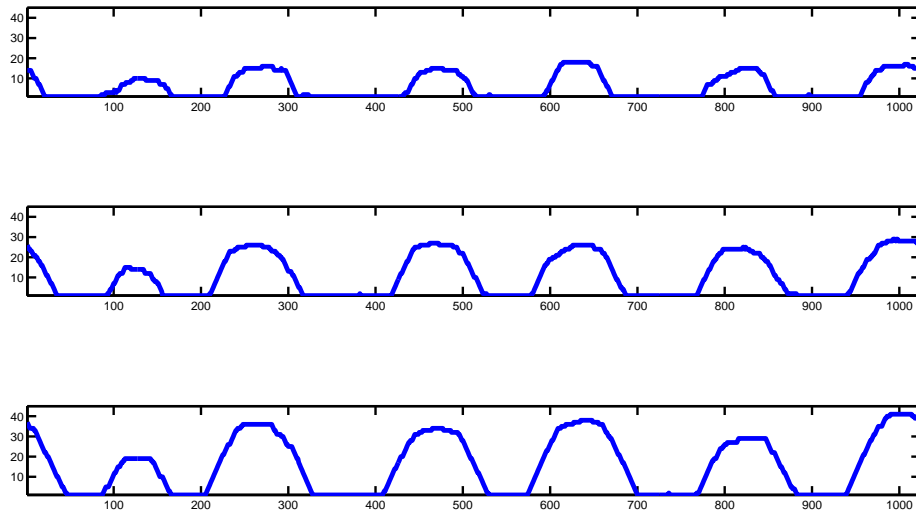
Figure 6: Evolution of film growth with $F = 0.08$ monolayers/second, $T = 600$ K, $R_G < 10^{-2}$ and $R_L < 10^{-2}$. The total number of events was 10^8. There were 699 global elastic computations. The rejection rate was approximately 0.015. The total computation time was 17 hours.
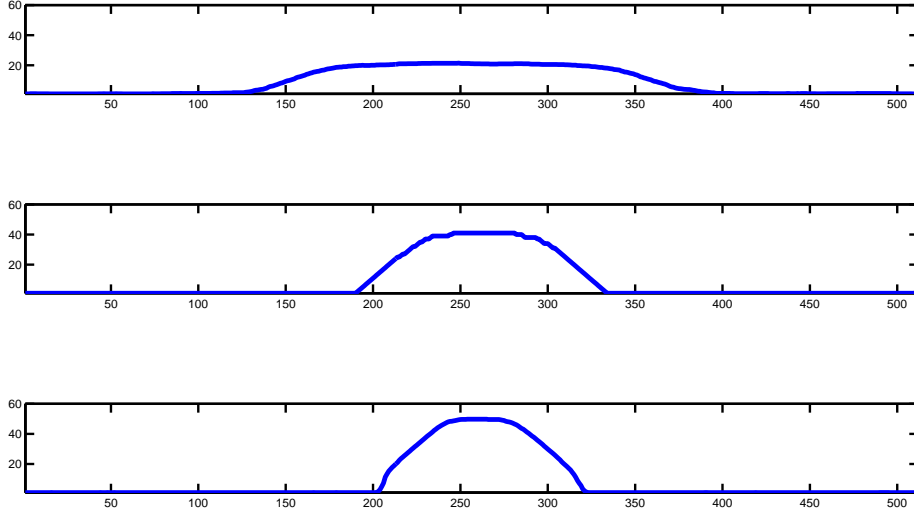
Figure 7: Equilibrium shapes for different misfits at $T = 450$ K, $R_G < 10^{-2}$ and $R_L < 10^{-2}$. The system was annealed for 10^8 events. Then ten different realizations were averaged. Each of these realizations were separated by 10^6 events. In the upper figure ($\mu = 0.02$) no facets appear to be present, whereas the middle figure ($\mu = 0.04$) shows three facets and bottom one ($\mu = 0.06$) shows five.

tolerances are sufficient. It is noteworthy that in both cases we have reduced the total number of global elastic computations dramatically (see data in figure captions). Figure 6 shows the same case as Figure 4 except that the deposition rate has been decreased to 0.08 monolayers/sec. Not surprisingly the islands are more spread out.

4.3   Equilibrium Profiles

We examine the equilibrium shapes of a single island for various amounts of misfit. The initial condition consists of an island whose profile is a rectangle; the system is then evolved for 10^7 events, sampled 10 times and ensemble averaged. The samples were separated by 10^6 events. The results are shown in Figure 7. In the case $\mu = 0$ (not shown) the equilibrium profile would be a straight line since this minimizes the surface area. However as the misfit increases the elastic contribution to the energy makes it increasingly favorable to have island formation. The results for $\mu = 0.02$ suggest the formation of an island with no facets and wetting angle of zero. When μ is increased to 0.04 the island now has three facets—one $(0, 1)$ facet and two

$(1, 1)$ facets. When μ is further increased to 0.06, the results seem to indicate the formation of two $(2, 1)$ facets.

5   Analysis of Energy Localization

In the remaining sections we aim to provide theoretical insight into the energy localization method based on the use of the continuum theory of elasticity. We begin in this section by first formulating a continuum limit of the discrete elastic energy density (6) which will be used to provide a continuum version of the discrete mechanical system (9). While the integrals (36) and (37) representing the errors in the truncaton and energy localization approxima-tions, repsectively, are more general, the theorems consider a system where a substrate occupying the entire half-plane $y < 0$ is completely covered by a small-amplitude film $0 \leq y \leq h(x)$ of uniform height H for $|x| > \lambda$. This scenario is meant to characterized an isolated island sitting on an unbounded and otherwise flat film on a flat substrate. The periodic case with more arbi-trary topography would also be nice to consider, but we have no results for this at this time.

5.1   Continuum Limit

We measure the horizontal and vertical displacement of the film, $\mathbf{u}$, relative to a reference configuration in which a flat film on the substrate is in mechanical equilibrium. With this choice, a film with zero displacement experiences an inherent "stress-free" strain. Following our earlier notation, the union of the film and the substrate will be denoted by Ω. The boundary between the film and vacuum is denoted $\partial\Omega$.

The equations of continuum elasticity are more easily manipulated with the aid of index notation, where we denote the components of the displace-ment $\mathbf{u} = (u, v)$ as (u_1, u_2). We also find it convenient to define the strain parameters

$$\alpha_1 = (a_g - a_s) \quad \text{and} \quad \alpha_2 = (a_g - a_L)$$

and make use of the Heaviside function

$$\theta(y) = \begin{cases} 0 & \text{if } y < 0 \\ 1 & \text{if } y > 0. \end{cases}$$

Finally we use approximations such as

$$u_{i+1,j} - u_{i,j} \approx \partial_1 u_1$$

in (6) to pass to the continuum limit, which then gives the elastic energy density

$$
\begin{aligned}
w \;=\; & \tfrac{1}{2}(k_L + k_D)\left[(\partial_1 u_1 - \alpha_1\theta(y))^2 + ((\partial_2 u_2 - \alpha_2\theta(y))^2\right] + \\
& k_D\,(\partial_1 u_1 - \alpha_1\theta(y))\,(\partial_2 u_2 - \alpha_2\theta(y)) + \\
& \tfrac{1}{2}k_D(\partial_2 u_1 + \partial_1 u_2)^2.
\end{aligned}
$$

This expression corresponds to a material with cubic symmetry; for the material to also be isotropic one requires $k_L = 2k_D$ [6]. Restricting our attention to materials that are both isotropic and cubic, we may then write the energy density as

$$
\begin{aligned}
w \;=\; & \tfrac{3}{2}k_D\left[(\partial_1 u_1)^2 + (\partial_2 u_2)^2\right] + k_D(\partial_1 u_1)(\partial_2 u_2) + k_D(\partial_2 u_1 + \partial_1 u_2)^2. \\
& -3k_D\left[\alpha_1\partial_1 u_1 + \alpha_2\partial_2 u_2\right]\theta(y) - k_D\left[\alpha_1\partial_2 u_2 + \alpha_2\partial_1 u_1\right]\theta(y) \\
& + \tfrac{1}{2}k_D\left[3(\alpha_1^2 + \alpha_2^2) + 2\alpha_1\alpha_2\right]\theta(y)
\end{aligned}
\tag{16}
$$

This form is consistent with the energy density of an isotropic material whose Lamé constants are both equal to $2k_D$ [17]. Finally, it is convenient to choose units so that $k_D = 1$. The results proven below are readily generalized for arbitrary Lamé constants.

Eq. (16) can be written in a more compact way by first defining

$$
\overline{T}_{ij} = \begin{pmatrix} -\sigma_1 & 0 \\ 0 & -\sigma_2 \end{pmatrix} \theta(y),
\tag{17}
$$

where

$$
\begin{aligned}
\sigma_1 &= 3\alpha_1 + \alpha_2, \\
\sigma_2 &= 3\alpha_2 + \alpha_1.
\end{aligned}
\tag{18}
$$

Combining (17) with the summation convention we can now write (16) as

$$
\begin{aligned}
w \;=\; & \tfrac{1}{2}(\partial_i u_j)^2 + \tfrac{1}{2}(\partial_i u_j)(\partial_j u_i) + \tfrac{1}{2}(\partial_i u_i)(\partial_j u_j) \\
& + \overline{T}_{ij}\partial_i u_j + \tfrac{1}{2}\left[3(\alpha_1^2 + \alpha_2^2) + 2\alpha_1\alpha_2\right]\theta(y).
\end{aligned}
\tag{19}
$$

21

The stress tensor, denoted T_{ij}, is given by

$$T_{ij} = \frac{\partial w}{\partial u_{i,j}},$$

where $u_{i,j} \equiv \partial_j u_i$. This is related to the strain tensor E_{ij} by

$$T_{ij} = 2E_{ij} + \delta_{ij}E_{kk},$$

where

$$E_{ij} = \overline{E}_{ij} + \widetilde{E}_{ij},$$

$$\overline{E}_{ij} = \begin{pmatrix} -\alpha_1 & 0 \\ 0 & -\alpha_2 \end{pmatrix} \theta(y),$$

and

$$\widetilde{E}_{ij} = \frac{1}{2}(\partial_i u_j + \partial_j u_i).$$

We note that the elastic energy density can be compactly written as

$$w = \frac{1}{2}E_{ij}T_{ij}.$$

It will be convenient later to observe that the stress tensor can also be broken into an intrinsic and relative piece

$$T_{ij} = \overline{T}_{ij} + \widetilde{T}_{ij},$$

where

$$\widetilde{T}_{ij} = 2\widetilde{E}_{ij} + \delta_{ij}\widetilde{E}_{kk}. \tag{20}$$

Mechanical equilibrium requires

$$\partial_i T_{ij} = 0, \quad \mathbf{x} \in \Omega$$

$$T_{ij}n_j = 0, \quad \mathbf{x} \in \partial\Omega.$$

From this, one sees that the stress-free strain term could give rise to a singularity in the second equation at the film/substrate interface. However this is not the case here. Since we have chosen our reference configuration so that a flat film is in mechanical equilibrium, it follows from (3), (4), and (18) that

$$\sigma_2 = 0.$$

One then obtains the usual equations of linear elasticity

$$\partial_i^2 u_j + 2\partial_j\partial_k u_k = 0, \quad \mathbf{x} \in \Omega \tag{21}$$

$$\widetilde{T}_{ij}n_j = \sigma_1 n_1 \delta_{i1}, \quad \mathbf{x} \in \partial\Omega, \tag{22}$$

$$u_i \rightarrow 0, \quad |\mathbf{x}| \rightarrow \infty. \tag{23}$$

5.2   Principle of Energy Localization

In this section, we use the continuum limit of the discrete model to explain why calculations of elastic energy differences with the energy localization method are much more accurate than those calculated using truncated integrals of the full elastic solutions. Naively, one might have expected the opposite.

We begin with a displacement field $\mathbf{u}$ that satisfies (21–23) on the original domain Ω. The removal of an atom is modeled using a modified domain $\Omega^a \subset \Omega$ that differs from Ω in a finite region at the top of the film.

The total elastic energy stored in any *finite* region $\Omega_\rho \subset \Omega$ is the integral of the energy density:

$$W(\mathbf{u}; \Omega_\rho) \ = \ \int_{\Omega_\rho} w \, d\mathbf{x}. \tag{24}$$

For unbounded domains, we define the elastic energy barrier as follows. Let $\Omega_\rho := \{\Omega \cap \{|\mathbf{x}| < \rho\}\}$ and similarly for Ω_ρ^a (see Figure 8). The elastic energy barrier is then

$$\Delta W = \lim_{\rho \to \infty} \left[W(\mathbf{u}; \Omega_\rho) - W(\mathbf{u}^a; \Omega_\rho^a) \right], \tag{25}$$

where $\mathbf{u}^a$ is the atom-off solution (i.e., $\mathbf{u}^a$ satisfies that same system as $\mathbf{u}$ but on a domain with a modified surface; see Figure 8.)

The essence of the energy localization method is to approximate the atom-off solution $\mathbf{u}^a$ with a solution on a finite domain Ω_ρ^a using boundary data that is constrained to agree with the atom-on displacement field $\mathbf{u}$ along the lower boundary:

$$\mathbf{u}_\rho^a = \mathbf{u}, \quad \mathbf{x} \in \Gamma_\rho. \tag{26}$$

Our approximation for atom-off displacement field is then

$$\mathbf{w} = \begin{cases} \mathbf{u}_\rho^a & \text{if } |\mathbf{x}| < \rho \\ \mathbf{u} & \text{if } |\mathbf{x}| \geq \rho. \end{cases} \tag{27}$$

Our approximation for the elastic energy barrier is

$$\Delta W_L = W(\mathbf{u}; \Omega_\rho) - W(\mathbf{u}_\rho^a; \Omega_\rho^a). \tag{28}$$

The continuum analogue of the residual is

$$\mathbf{r} = \nabla \cdot \widehat{\mathbf{T}}(\mathbf{w} - \mathbf{u}^a) = \nabla \cdot \widehat{\mathbf{T}}\mathbf{w},$$

where
$$\widehat{\mathbf{T}}\mathbf{u} = \partial_i u_j + \partial_j u_i + \delta_{ij}\partial_k u_k.$$

This quantity is zero, except on Γ_ρ, where it is equivalent to
$$\mathbf{r} = (\widetilde{\mathbf{T}}_\rho^a - \widetilde{\mathbf{T}})\mathbf{n}\delta_{\Gamma_\rho}, \tag{29}$$

with δ_{Γ_ρ} being a Dirac delta function concentrated on the curve Γ_ρ; $\widetilde{\mathbf{T}}$ and $\widetilde{\mathbf{T}}_\rho^a$ are defined using (20) with displacement fields given by $\mathbf{u}$ and $\mathbf{u}_\rho^a$ respectively.

Therefore we see that the residual per unit length on Γ_ρ is $(\widetilde{\mathbf{T}}_\rho^a - \widetilde{\mathbf{T}})\mathbf{n}$, and hence we conclude the continuum version of (13) is
$$R_L = \max_{\Gamma_\rho} \left| (\widetilde{\mathbf{T}}_\rho^a - \widetilde{\mathbf{T}})\mathbf{n} \right|.$$

For the situation we now consider the film profile is $H + h(x)$, where $h(x)$ is smooth and of small amplitude. More specifically we take h and its derivative, h_x, to be $O(\epsilon), \epsilon \ll 1$. The theorems stated below are valid to $O(\epsilon^2)$ and correspond to Observations 1, 2 and 3 in Section 3.2.

THEOREM 1 - Residual Estimate. *Suppose that $h(x)$ is a compactly supported function whose support includes $x = 0$. Further, suppose that $h(x)$ is modified by a localized change centered at $x = 0$ then the following is true*

$$R_L = O(\epsilon\rho^{-2}) \quad \text{as} \quad \rho \to \infty.$$

This justifies the use of the residual as a convergence criterion. We shall also prove

THEOREM 2 - Principle of Energy Localization. *Under the same hypotheses of Theorem 1 the following is true*

$$\Delta W = \Delta W_L(1 + O(\rho^{-2})) \quad \text{as} \quad \rho \to \infty,$$

where ΔW and ΔW_L are defined by (25) and (28) respectively.

This explains the high accuracy of our method. We will see that this can be traced to a fortunate canceling of a large part of the error on the lower boundary of the expanding box.

Naively, one might expect an energy barrier approximation based on a simple truncation of the energy integrals using the exact displacement fields $\mathbf{u}$ and $\mathbf{u}^a$,

$$\Delta W_T = W(\mathbf{u}; \Omega_\rho) - W(\mathbf{u}^a; \Omega_\rho^a), \tag{30}$$

24

would provide a better approximation, but our final theorem shows that this is not the case:

THEOREM 3 - Nonlocality of the Energy Density. *Under the same hypotheses of Theorem 1 the following is true*

$$\Delta W = \Delta W_T (1 + O(H\rho^{-1})) \quad as \quad \rho \to \infty.$$

where ΔW and ΔW_T are defined by (25) and (30) respectively.

Not only does this error decay slowly as the region expands, but it gets larger as the film thickens. In view of this result, the accuracy of the energy localization approximation is rather surprising, but it is this rather large error term that is precisely cancelled when the displacement is constrained by (26).

Rickman & Srolovitz[27] considered a somewhat similar problem. An important difference, however, is that we consider a film with stress free strain.

5.3 Proof of Theorems

The proofs of all three theorems rely on converting (24) to boundary integral form. We begin by inserting (19) to find

$$
\begin{aligned}
W(\mathbf{u}; \Omega_\rho) &= \frac{1}{2} \int_{\Omega_\rho} \partial_i \left(u_j \partial_i u_j + u_j \partial_j u_i + u_j \delta_{ij} \partial_k u_k \right) d\mathbf{x} \\
&\quad - \frac{1}{2} \int_{\Omega_\rho} u_j \left(\partial_i^2 u_j + 2 \partial_{ij}^2 u_i \right) d\mathbf{x} \\
&\quad + \int_{\Omega_\rho} \partial_i (\overline{T}_{ij} u_j) \, d\mathbf{x} + C \int_{\Omega_\rho} \theta(y) \, d\mathbf{x}. \qquad (31)
\end{aligned}
$$

where $C = \frac{1}{2} \left[3(\alpha_1^2 + \alpha_2^2) + 2\alpha_1\alpha_2 \right]$. The second integral vanishes owing to (21), the fourth is proportional to the area/volume of the film Ω_F contained within Ω_ρ and the remaining two can be converted to boundary integrals of surface forces:

$$
W(\mathbf{u}; \Omega_\rho) = \frac{1}{2} \int_{\partial\Omega_\rho} u_j \widetilde{T}_{ij} n_i \, dS + \int_{\partial\Omega_\rho} u_j \overline{T}_{ij} n_i \, dS + C |\Omega_F \cap \Omega_\rho|. \quad (32)
$$

A similar expression gives $W(\mathbf{u}; \Omega_\rho^a)$. Note that for the portion of the boundary coinciding with the surface of the film, (22) gives $\widetilde{T}_{ij} n_i = -\overline{T}_{ij} n_i$, so that,
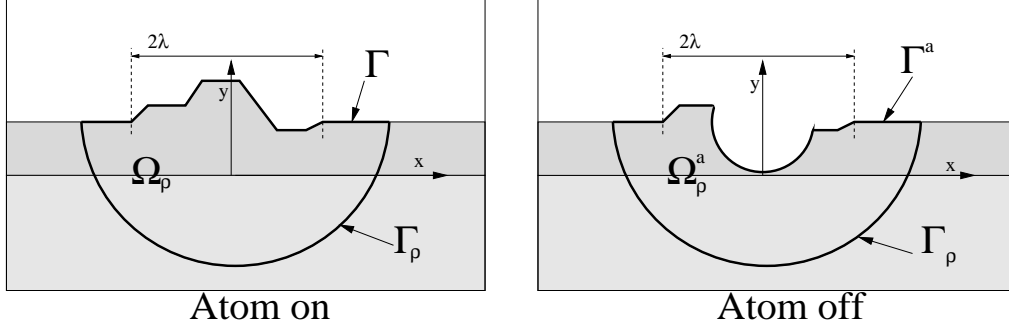
Figure 8: Schematic for the energy calculations in the case where an atom has been removed

in the limit, (25) gives

$$\Delta W \;=\; \frac{1}{2}\int_{\partial\Omega} u_j \overline{T}_{ij} n_i \, dS - \frac{1}{2}\int_{\partial\Omega^a} u_j^a \overline{T}_{ij} n_i \, dS + C|\Omega\backslash\Omega^a|.$$

From this point forward, we find it simpler to work with this expression in vector form

$$\Delta W \;=\; \frac{1}{2}\int_{\partial\Omega} \mathbf{u}\cdot\overline{\mathbf{T}}\mathbf{n}\, dS - \frac{1}{2}\int_{\partial\Omega^a} \mathbf{u}^a\cdot\overline{\mathbf{T}}\mathbf{n}\, dS + C|\Omega\backslash\Omega^a|. \qquad (33)$$

Note that since $\sigma_2 = 0$ these integrals vanish over any portion of the boundary that is horizontal.

Next, we compare the two approximations ΔW_T and ΔW_L for ΔW. In the first, we use the displacement fields, $\mathbf{u}$ and $\mathbf{u}^a$ without further approximation but truncate the domain of integration in the energy functional. This truncation approximation will be used to demonstrate the long range nature of the elastic energy density in the film. In the second approximation the change in elastic energy is localized within the truncated domain by using the approximation (27) that constrains displacement field, $\mathbf{u}_\rho^a$, to agree with the atom-on displacement field, $\mathbf{u}$, on Γ_ρ. This is the continuum analogue of the change in energy used by the expanding box method.

For the truncation approximation we get three contributions to the binding energy analogous to those in (33) plus additional contributions in the form of integrals over portions of the boundary that are in the interior of the film/substrate:

$$\Delta W_T \;=\; \frac{1}{2}\int_{\Gamma} \mathbf{u}\cdot\overline{\mathbf{T}}\mathbf{n}\, dS - \frac{1}{2}\int_{\Gamma^a} \mathbf{u}^a\cdot\overline{\mathbf{T}}\mathbf{n}\, dS + C|\Omega\backslash\Omega^a| +$$

26

$$\frac{1}{2} \int_{\Gamma_\rho} (\mathbf{u} \cdot \widetilde{\mathbf{T}} - \mathbf{u}^a \cdot \widetilde{\mathbf{T}}^a)\mathbf{n}\, dS + \int_{\Gamma_\rho} (\mathbf{u} - \mathbf{u}^a) \cdot \overline{\mathbf{T}}\mathbf{n}\, dS, \qquad (34)$$

where we have decomposed the boundaries $\partial\Omega_\rho = \Gamma \cup \Gamma_\rho$ and $\partial\Omega_\rho^a = \Gamma^a \cup \Gamma_\rho$ into surface and subsurface components. Note that the last integral vanishes over the portion of Γ_ρ in the substrate.

For ΔW_L this last integral vanishes completely as a result of (26) and it is this cancellation, we shall see, that leads to a significantly better approximation:

$$
\begin{aligned}
\Delta W_L &= \frac{1}{2} \int_\Gamma \mathbf{u} \cdot \overline{\mathbf{T}}\mathbf{n}\, dS - \frac{1}{2} \int_{\Gamma^a} \mathbf{u}_\rho^a \cdot \overline{\mathbf{T}}\mathbf{n}\, dS + C|\Omega\backslash\Omega^a| + \\
&\quad \frac{1}{2} \int_{\Gamma_\rho} \mathbf{u} \cdot (\widetilde{\mathbf{T}} - \widetilde{\mathbf{T}}_\rho^a)\mathbf{n}\, dS.
\end{aligned}
\qquad (35)
$$

The error $E_T = \Delta W - \Delta W_T$ for the truncation approximation is

$$
\begin{aligned}
E_T &= \frac{1}{2} \int_{\partial\Omega\backslash\Gamma} (\mathbf{u} - \mathbf{u}^a) \cdot \overline{\mathbf{T}}\mathbf{n}\, dS - \\
&\quad \frac{1}{2} \int_{\Gamma_\rho} (\mathbf{u} \cdot \widetilde{\mathbf{T}} - \mathbf{u}^a \cdot \widetilde{\mathbf{T}}^a)\mathbf{n}\, dS - \int_{\Gamma_\rho} (\mathbf{u} - \mathbf{u}^a) \cdot \overline{\mathbf{T}}\mathbf{n}\, dS,
\end{aligned}
\qquad (36)
$$

while the error $E_L = \Delta W - \Delta W_L$ for the energy localization approximation is

$$
\begin{aligned}
E_L &= \frac{1}{2} \int_{\partial\Omega\backslash\Gamma} (\mathbf{u} - \mathbf{u}^a) \cdot \overline{\mathbf{T}}\mathbf{n}\, dS + \\
&\quad \frac{1}{2} \int_{\Gamma^a} (\mathbf{u}_\rho^a - \mathbf{u}^a) \cdot \overline{\mathbf{T}}\mathbf{n}\, dS - \frac{1}{2} \int_{\Gamma_\rho} \mathbf{u} \cdot (\widetilde{\mathbf{T}} - \widetilde{\mathbf{T}}_\rho^a)\mathbf{n}\, dS.
\end{aligned}
\qquad (37)
$$

5.3.1 Approximate Evaluation of Energy Formulas

The reader is reminded that the film profile for Ω is $h(x)$ and we denote the film profile for Ω^a as $h^a(x)$.

In this section we present a situation where we can provide asymptotic expressions for (36) and (37). We take the film profile to be $H + h(x)$ where $h(x) = 0$ for $|x| > \lambda$. In addition shall take h and h_x to be $O(\epsilon)$ for $|x| < \lambda$ where h_x is the derivative of h. This implies we can use the small slope approximation for the surface normal

$$\mathbf{n} = \frac{(-h_x, 1)^T}{\sqrt{h_x^2 + 1}} = \mathbf{e}_2 - h_x \mathbf{e}_1 + O(\epsilon^2)$$

and approximate the film/vacuum interface as flat when applying the stress boundary conditions. It is convenient to chose our coordinate system so the film/vacuum interface is located at $y = 0$. This implies that the film/substrate interface is now at $y = -H$ and (17) with $\sigma_2 = 0$ becomes

$$\overline{T}_{ij} = \begin{pmatrix} -\sigma_1 & 0 \\ 0 & 0 \end{pmatrix} \theta(y + H). \tag{38}$$

The boundary condition (22), to leading order, is

$$\widetilde{\mathbf{T}}\mathbf{n} = (\widehat{\mathbf{T}}\mathbf{u})\mathbf{e}_2 = -\sigma_1 h_x \mathbf{e}_1, \quad \text{at } y = 0, \tag{39}$$

where $\widehat{\mathbf{T}}$ is defined by (41). This replaces the system (21–23) with the half-plane problem

$$
\begin{aligned}
\nabla^2 \mathbf{u} + 2\nabla(\nabla \cdot \mathbf{u}) &= 0, \quad \text{for } y < 0 \\
(\widehat{\mathbf{T}}\mathbf{u})\mathbf{e}_2 &= -\sigma_1 h_x \mathbf{e}_1, \quad \text{at } y = 0, \\
\mathbf{u} &\to 0, \quad |\mathbf{x}| \to \infty.
\end{aligned}
\tag{40}
$$

where $\widehat{\mathbf{T}}$ is the operator defined through the relation

$$\widetilde{\mathbf{T}} = \widehat{\mathbf{T}}\mathbf{u},$$

which implies

$$\widehat{\mathbf{T}}\mathbf{u} = \partial_i u_j + \partial_j u_i + \delta_{ij}\partial_k u_k. \tag{41}$$

The solution to (40) can be deduced by following the derivation in [17] and one finds

$$\mathbf{u} = \sigma_1 \int_{-\lambda}^{\lambda} \mathbf{f}(x - s, y) h(s) ds, \tag{42}$$

where

$$\mathbf{f} = \frac{1}{4\pi(x^2 + y^2)^2} \begin{bmatrix} x(3x^2 - y^2) \\ y(3y^2 - x^2) \end{bmatrix} = \partial_x \mathbf{g}$$

and $\mathbf{g}$ is the Green's function for the problem

$$
\begin{aligned}
\nabla^2 \mathbf{g} + 2\nabla(\nabla \cdot \mathbf{g}) &= 0, \quad \text{for } y < 0 \\
(\widehat{\mathbf{T}}\mathbf{g})\mathbf{e}_2 &= \delta(x)\,\mathbf{e}_1, \quad \text{at } y = 0, \\
\nabla \mathbf{g} &\to 0, \quad |\mathbf{x}| \to \infty.
\end{aligned}
\tag{43}
$$

An analogous expression, with $h(x) \to h^a(x)$ holds for $\mathbf{u}^a$. In [11] a similar appoach is used to analyze slightly undulating surfaces.

To prove the theorems we need to estimate the integrals that appear in (36) and (37). The first of these integrals is

$$I_1 = \frac{1}{2} \int_{\partial\Omega\backslash\Gamma} (\mathbf{u} - \mathbf{u}^a) \cdot \overline{\mathbf{T}}\mathbf{n} \, dS.$$

Since the film/vacuum interface is flat for $|\mathbf{x}| > \lambda$, $\overline{\mathbf{T}}\mathbf{n} = 0$ for this portion of the interface. As a consequence, we have $I_1 = 0$ for $\rho > \lambda$. In §5.3.2 we will establish the following results for the remaining integrals:

$$I_2 = \frac{1}{2} \int_{\Gamma_\rho} (\mathbf{u} \cdot \widetilde{\mathbf{T}} - \mathbf{u}^a \cdot \widetilde{\mathbf{T}}^a)\mathbf{n} \, dS = O(\epsilon^2/\rho^2), \tag{44}$$

$$I_3 = \int_{\Gamma_\rho} (\mathbf{u} - \mathbf{u}^a) \cdot \overline{\mathbf{T}}\mathbf{n} \, dS = O(\epsilon H/\rho), \tag{45}$$

$$I_4 = \frac{1}{2} \int_{\Gamma^a} (\mathbf{u}_\rho^a - \mathbf{u}^a) \cdot \overline{\mathbf{T}}\mathbf{n} \, dS = O(\epsilon/\rho^2), \tag{46}$$

and

$$I_5 = \frac{1}{2} \int_{\Gamma_\rho} \mathbf{u} \cdot (\widetilde{\mathbf{T}} - \widetilde{\mathbf{T}}_\rho^a)\mathbf{n} \, dS = O(\epsilon^2/\rho^2). \tag{47}$$

We use the fact that $I_1 = 0$ and combine this with the estimates for I_2 and I_3 in (36) to obtain

$$E_T = O(\epsilon H/\rho). \tag{48}$$

Based on our assumptions concerning the film profile it follows that $\Delta W = O(\epsilon)$. Combining this with (48) yields Theorem 3. Next, we use (46), (47) and $I_1 = 0$ to find

$$E_L = O(\epsilon/\rho^2), \tag{49}$$

which combined with $\Delta W = O(\epsilon)$ gives Theorem 2. Finally, it is shown in §5.3.2 (see Eqs. 56 and 61) that

$$(\widetilde{\mathbf{T}} - \widetilde{\mathbf{T}}_\rho^a) = O(\epsilon/\rho^2),$$

which gives Theorem 1.

5.3.2 Proof of Estimates

In this section we establish the estimates used in the previous section.

Proof of Eq. 44. We begin by recalling (42) and its analogue

$$\mathbf{u}^a = \sigma_1 \int_{-\lambda}^{\lambda} \mathbf{f}(x - s, y) h^a(s) ds.$$

We need to evaluate $\mathbf{u}$ on the lower semi-circle of radius ρ centered at $(\mathbf{x} = (0,0))$. If we let $(x, y) = \rho(\cos \phi, \sin \phi)$ and substitute this into (42) and its analogue and expand in $1/\rho$ we obtain

$$\mathbf{u}\big|_{|\mathbf{x}|=\rho} = O(\epsilon/\rho) \quad \text{and} \quad \mathbf{u}^a\big|_{|\mathbf{x}|=\rho} = O(\epsilon/\rho), \tag{50}$$

where we have used the fact that $h = O(\epsilon)$. A similar argument shows that

$$\widetilde{\mathbf{T}}\big|_{|\mathbf{x}|=\rho} = O(\epsilon/\rho^2) \quad \text{and} \quad \widetilde{\mathbf{T}}^a\big|_{|\mathbf{x}|=\rho} = O(\epsilon/\rho^2). \tag{51}$$

If we combine (50) and (51) in the expression for I_2 we obtain the result.

Proof of Eq. 45. We restate (45):

$$\int_{\Gamma_\rho} (\mathbf{u} - \mathbf{u}^a) \cdot \overline{\mathbf{T}} \mathbf{n} \, dS = O(\epsilon H/\rho).$$

This result is obtained by noting that $\overline{\mathbf{T}}\mathbf{n}$ is zero in the substrate, so that the only contribution occurs in the film. Further, since for $\rho/H \gg 1$ the length of Γ_ρ in the film is proportional to H. This combined with (50) gives (45).

Proof of Eq. 46. Recall that

$$I_4 = \frac{1}{2} \int_{\Gamma^a} (\mathbf{u}^a_\rho - \mathbf{u}^a) \cdot \overline{\mathbf{T}} \mathbf{n} \, dS.$$

We now use (38), the small slope approximation and the compact support of h_x to rewrite I_4 as

$$I_4 = \frac{1}{2} \int_{-\lambda}^{\lambda} (\mathbf{u}^a_\rho - \mathbf{u}^a) \cdot \mathbf{e}_1 \sigma_1 h^a_x \, dx. \tag{52}$$

30

To proceed further we let $\mathbf{w} = \mathbf{u}_\rho^a - \mathbf{u}^a$, $\widetilde{\mathbf{u}} = \mathbf{u} - \mathbf{u}^a$ and $\widetilde{h} = h - h^a$. Since $\mathbf{u}_\rho^a$ and $\mathbf{u}^a$ satisfy the first two equations of (40) with h_x replace by h_x^a and since $\mathbf{u}_\rho^a(|\mathbf{x}| = \rho) = \mathbf{u}(|\mathbf{x}| = \rho)$ the following is true:

$$
\begin{aligned}
\nabla^2 \mathbf{w} + 2\nabla(\nabla \cdot \mathbf{w}) &= 0 \quad \text{for } y < 0 \text{ and } |\mathbf{x}| < \rho \\
(\widehat{\mathbf{T}}\mathbf{w})\mathbf{e}_2 &= 0 \quad \text{at } y = 0 \\
\mathbf{w} &= \widetilde{\mathbf{u}} \quad |\mathbf{x}| = \rho \quad \text{and} \quad y < 0.
\end{aligned}
\tag{53}
$$

Next we note that $\mathbf{u}$ satisfies (40) and $\mathbf{u}^a$ satisfies (40) with h_x replaced by h_x^a. This means that we can appeal to (42) to find

$$
\widetilde{\mathbf{u}} = \sigma_1 \int_{-\lambda}^{\lambda} \mathbf{f}(x - s, y)\widetilde{h}(s)ds.
$$

Notice that the compact support of h and h^a is not strictly required for this integral, as $\widetilde{h}$ will have this property more generally. We need to evaluate $\widetilde{\mathbf{u}}$ on the lower semi-circle of radius ρ centered at $(0,0)$:

$$
\widetilde{\mathbf{u}}(\rho\cos\phi, \rho\sin\phi) = \sum_{n=0}^{\infty} \frac{m_n \mathbf{c}_n(\phi)}{\rho^{n+1}},
\tag{54}
$$

where $m_n = \displaystyle\int_{-\lambda}^{\lambda} s^n \widetilde{h}(s)ds$ and

$$
\mathbf{c}_n(\phi) = \begin{pmatrix} (2-n)\cos[(n+1)\phi] + (n+1)\cos[(n+3)\phi] \\ -(n+2)\sin[(n+1)\phi] + (n+1)\sin[(n+3)\phi] \end{pmatrix}.
$$

We can now write the solution of (53) as

$$
\mathbf{w} = \sum_{n=0}^{\infty} \frac{m_n \mathbf{w}^{(n)}(\mathbf{x}/\rho)}{\rho^{n+1}},
\tag{55}
$$

where $\mathbf{w}_n$ satisfies (53) except the last boundary condition is replaced by

$$
\mathbf{w}^{(n)} = \mathbf{c}_n \quad \text{for} \quad |\mathbf{x}| = 1 \quad \text{and} \quad y < 0.
$$

Due to the antisymmetry of $\mathbf{c}_0 \cdot \mathbf{e}_1$ about $\phi = \pi/2$ we infer $\mathbf{e}_1 \cdot \mathbf{w}^{(0)}(0,0) = 0$; this combined with (55) gives

$$
\mathbf{e}_1 \cdot \mathbf{w}(0,0) = O(\rho^{-2}).
$$

It also follows from differentiating (55) that

$$\partial_x(\mathbf{e}_1 \cdot \mathbf{w})(0,0) = O(\rho^{-2}).$$

Therefore we conclude

$$\mathbf{e}_1 \cdot \mathbf{w}(x,0) = O(\rho^{-2}) \quad \text{provided} \quad |x| = O(1).$$

If we substitute the above result into (52) and use the fact that $h_x = O(\epsilon)$ we obtains (46).

Proof of Eq. 47. Finally we need to estimate

$$\frac{1}{2}\int_{\Gamma_\rho} \mathbf{u} \cdot (\widetilde{\mathbf{T}} - \widetilde{\mathbf{T}}^a_\rho)\mathbf{n}\, dS.$$

If we let $\mathbf{v} = \mathbf{u} - \mathbf{u}^a_\rho$ then the formula above becomes

$$\frac{1}{2}\int_{\Gamma_\rho} \mathbf{u} \cdot (\widehat{\mathbf{T}}\mathbf{v})\mathbf{n}\, dS. \tag{56}$$

To estimate $\widehat{\mathbf{T}}\mathbf{v}$ we proceed as follows. We first observe that $\mathbf{v}$ satisfies the system

$$
\begin{aligned}
\nabla^2\mathbf{v} + 2\nabla(\nabla \cdot \mathbf{v}) &= 0 \quad \text{for } y < 0 \text{ and } |\mathbf{x}| < \rho \\
(\widehat{\mathbf{T}}\mathbf{v})\mathbf{e}_2 &= -\sigma_1\widetilde{h}_x\mathbf{e}_1 \quad y = 0 \text{ and } |\mathbf{x}| < \rho. \\
\mathbf{v} &= 0 \quad |\mathbf{x}| = \rho \text{ and } y < 0.
\end{aligned}
\tag{57}
$$

It is useful to introduce the following auxiliary system defined on a semi circle of radius one:

$$
\begin{aligned}
\nabla^2\mathbf{w} + 2\nabla(\nabla \cdot \mathbf{w}) &= 0 \quad \text{for } y < 0 \text{ and } |\mathbf{x}| < 1 \\
(\widehat{\mathbf{T}}\mathbf{w})\mathbf{e}_2 &= -\sigma_1 p_x\mathbf{e}_1, \quad \text{at } y = 0 \text{ and } |x| < 1, \\
\mathbf{w} &= 0 \quad |\mathbf{x}| = 1 \text{ and } y < 0,
\end{aligned}
\tag{58}
$$

where p_x is the derivative of an arbitrary function p and will be defined later. We write the solution as

$$\mathbf{w} = \int_{-1}^{1} \mathbf{f}_1(x - s, y)p(s)ds, \tag{59}$$

32

where $\mathbf{f}_1$ is the x-derivative of the Green's function for (58).

The system given by (57) will now be transformed into the form given by (58). This will be done by letting $\mathbf{x} = \rho \mathbf{x}'$, $\mathbf{v}' = \mathbf{v}(\rho \mathbf{x}')$ and $\widetilde{h}(\rho x') = \widetilde{h}'(x')$ to arrive at

$$
\begin{aligned}
\nabla'^2 \mathbf{v}' + 2\nabla'(\nabla' \cdot \mathbf{v}') &= 0 \quad \text{for } y' < 0 \text{ and } |\mathbf{x}'| < 1 \\
(\widehat{\mathbf{T}}'\mathbf{v}')\mathbf{e}_2 &= -\sigma_1 \widetilde{h}'_{x'} \mathbf{e}_1, \quad y' = 0 \text{ and } |x'| < 1 \\
\mathbf{v}' &= 0 \quad |\mathbf{x}'| = 1 \text{ and } y' < 0.
\end{aligned} \tag{60}
$$

Now set $p = \widetilde{h}'$ and and compare (60) with (58). It then follows from (59) that

$$
\mathbf{v}' = \int_{-\lambda/\rho}^{\lambda/\rho} \mathbf{f}_1(x' - s, y') \widetilde{h}'(s) ds,
$$

where we have used the fact that $\widetilde{h}$ is supported on $[-\lambda, \lambda]$. Since

$$
\widehat{\mathbf{T}}\mathbf{v} = \rho^{-1} \widehat{\mathbf{T}}'\mathbf{v}',
$$

we have

$$
\widehat{\mathbf{T}}\mathbf{v} = \frac{1}{\rho} \int_{-\lambda/\rho}^{\lambda/\rho} \widehat{\mathbf{T}}'\mathbf{f}_1(x' - s, y') \widetilde{h}'(s) ds = O(\epsilon/\rho^2). \tag{61}
$$

This follows because $\widehat{\mathbf{T}}'\mathbf{f}_1(x' - s, y') = O(1)$ and $\widetilde{h}'(s) = O(\epsilon)$, implying the integrand is $O(\epsilon)$. If we combine this with (50) and (56) we find

$$
\frac{1}{2} \int_{\Gamma_\rho} \mathbf{u} \cdot (\widetilde{\mathbf{T}} - \widetilde{\mathbf{T}}^a_\rho) \mathbf{n} \, dS = O(\epsilon^2/\rho^2).
$$

6   Summary

This paper has addressed the important and computationally challenging task of simulating heteroepitaxial growth using KMC. Following earlier studies, energy barriers for adatom diffusion were modeled as the difference in elastic energy for the system with and without the moving atom. In contrast to standard KMC, which is used for simulating epitaxial growth in the absence of strain, the principal challenge was to deal with the long range nature of the elastic interactions.

To this end, we introduced three new ideas. First, we implemented a rejection algorithm that relies on a computationally inexpensive estimate of

hopping rates to avoid a substantial fraction of the elastic updates. To further accelerate performance, we implemented a local approximation technique for the remaining elastic updates. We found that these localized calculations for the energy differences were highly accurate despite the fact that the energies themselves were far less accurate. Using the continuum analogue of the discrete model, we were able to explain this and derive estimates for the error as a function of the size of the local region. Finally, whenever an atom was added or removed from the lattice, we implemented a local iterative technique based on successive overrelaxation to update the displacement field in a sequence of nested domains until a convergence criteria was satisfied. This exploits the fact that changes to the system's configuration naturally propagate outward from the moving atom. These techniques were applied to $1 + 1$ dimensional KMC simulations in physically interesting regimes and found to be highly effective.

Acknowledgments

References

[1] R.J. Asaro and W.A. Tiller, Interface morphology development during stress-corrosion cracking .1. via surface diffusion, *Metall. Trans.* **3** 1789-& (1972).

[2] M. Biehl, M. Ahr, W. Kinzel, and F. Much, Kinetic Monte Carlo simulations of heteroepitaxial growth, *Thin Solid Films* **428**, 52-55 (2003).

[3] J.L. Blue, I. Beichl, and F. Sullivan, Faster Monte Carlo Simulations, *Phys. Rev. E* 867-868 (1995).

[4] R.E Caflsich, Y.J. Lee, S. Shu, Y.X. Xiao, and J. Xu, An application of multigrid methods for a discrete elastic model for epitaxial systems, *J. Comput. Phys.* **219**, 697-714 (2006).

[5] J. B. Diaz and L. E. Payne, Mean value theorems in the theory of elasticity, in *Proc. Third U.S. National Congress on Applied Mechanics*, ASME, New York, 293-303 (1958).

[6] P. Fratzl, O. Penrose, and J.L. Lebowitz, Modeling of phase separation in alloys with coherent elastic misfit, *J. Stat. Phys.* **95**, 1429-1503 (1999).

[7] L.B. Freund and F. Jonsdottir, Instability of a biaxially stressed thin-film on a substrate due to material diffusion over its free-surface, *J. Mech. Phys. Solids* **41** 1245-1264 (1993).

[8] L. B. Freund and S. Suresh, Thin Film Materials Cambridge University Press, 2003.

[9] H. Gao, In *Modern Theory of Anisotropic Elsasticity and Applications* ed. J.J. Wu, T.C.T. Ting, D.M. Barnett, p. 139 (1991). Philadelphia, SIAM.

[10] H. Gao, *Annu. Rev. Mater. Sci.* Surface roughening of heteroepitaxial thin films, **29** 173-209 (1999).

[11] H. Gao, *J. Mech. Phys. Solids.* Stress concentration at slightly undulating surfaces, **39** 443-458 (1991).

[12] W. Guo, T.P. Schulze, and W. E, Simulation of impurity diffusion in a strained nanowire using off-lattice KMC, *Commun. Comput. Phys.* **2**, 164-176 (2007).

[13] M.A. Grinfeld, instability of interface between nonhydrostatically stressed elastic body and melts, *Doklady Akademii Nauk SSSR* **290** 1358-1363 (1986).

[14] M. E. Gurtin, The Linear Theory of Elasticity, in *Handbook der Physik VIa/2*, Springer-Verlag, Berlin (1972).

[15] C.H. Lam, C.K. Lee, and L.M. Sander, Competing Roughening Mechanisms in Strained Heteroepitaxy: A Fast Kinetic Monte Carlo Study, *Phys. Rev. Lett.* **89**, 16102 (1-4) (2002).

[16] C.H. Lam, M.T. Lung, and L.M. Sander, Fast kinetic Monte Carlo simulation of strained heteroepitaxy in three dimensions, *J. Sci. Comput.* accepted for publication.

[17] L.D. Landau and E.M. Lifshitz, Theory of Elasticity, Pergamon Press, Oxford (1986).

[18] A. E. H. Love, A treatise on the mathematical theory of elasticity, Cambridge University Press, 1927.

[19] S. Lee, R.E. Caflsich, and Y.J. Lee. Exact artifical boundary conditions for continuum and discrete elasticity. *SIAM J. Appl. Math.* **66**, 1749-1775 (2006).

[20] M.T. Lung, C.H. Lam, and L.M. Sander, Island, pit, and groove formation in strained heteroepitaxy, *Phys. Rev. Lett.* **95** Art. No. 086102 (2005).

[21] F. Much, M. Ahr, M. Biehl, and W.Kinzel, A Kinetic Monte Carlo method for the simulation of heteroepitaxial growth, *Comput. Phys. Commun.* **147**, 226-229 (2002).

[22] F. Much and M. Biehl, Simulation of wetting-layer and island formation in heteroepitaxial growth, *Europhysics Lett.* **63**, 14-20 (2003).

[23] B.G. Orr, D.A. Kessler, C.W. Snyder, and L.M. Sander, A model for strain-induced roughening and coherent island growth, *Europhysics Lett.* **19** 33-38 (1992).

[24] P. Politi, G. Grenet, A. Marty, A. Ponchet, and J. Villain Instabilities in crystal growth by atomic or molecular beams *Phys. Rep.* **324**, 271 (2000).

[25] C. Ratsch and A. Zangwill, Equilibrium theory of the Stranski-Krastanov epitaxial morphology, *Surface Science* **293**, 123-131 (1993).

[26] C.Ratsch, P.Šmilauer, D.D. Vvedensky, A. Zangwill, Mechanism for coherent island formation during heteroepitaxy, *J. Phys. I France* **6** 575-581 (1996).

[27] J.M. Rickman and D.J. Srolovitz, Defect interactions on solid surfaces, *Surface Science* **284**, 211-221 (1993).

[28] G. Russo and P. Smereka, Kinetic Monte Carlo simulation of strained epitaxial growth in three dimensions, *J Comput. Phys.* **214**, 809-828 (2006).

[29] G. Russo and P. Smereka, A multigrid-Fourier method for the computation of elastic fields with application to heteroepitaxy *Multiscale Model. Simu.* **5**, 130-148 (2006).

[30] A. J. C. B. Saint-Venant, Memoire sur la Torsion des Prismes, *Mem. Divers Savants* **14** 233-560 (1855).

[31] V.A. Shchukin and D. Bimberg, Spontaneous ordering of nanostructure on crystal surfaces *Rev. Mod. Phys.* **71** 1125 (1999).

[32] B.J. Spencer, P.W. Voorhees, and , S.H. Davis, Morphological instability in epitaxially strained dislocation free solid films, *Phys. Rev. Lett.* **67** 3696-3699 (1991).

[33] B.J. Spencer, P.W. Voorhees, and , S.H. Davis, Morphological instability in epitaxially strained dislocation-free solid films: Linear stability theory, *J. Appl. Phys.* **73** 4995-4970 (1993).

[34] B.J. Spencer, P.W. Voorhees, and J. Tersoff, Morphological instability theory for strained alloy film growth: The effect of compositional stresses and species-dependent surface mobilities on ripple formation during epitaxial film deposition, *Phys. Rev. B* **64**, Art. No. 235318 (2001).

[35] D.J. Srolovitz, On the stability of surfaces of stressed solids, *Acta. Metall.* **37** 621-625 (1989).

[36] Y.H. Tu and J. Tersoff, Origin of apparent critical thickness for island formation in heteroepitaxy, *Phys. Rev. Lett.* **93**, Art. No. 216101 (2004).

[37] Y.H. Tu and J. Tersoff, Coarsening, mixing, and motion: The complex evolution of epitaxial islands *Phys. Rev. Lett.* **98**, Art. No. 096103 (2007).

[38] R. Von Mises, On Saint Venant's Principle, *Bull. Amer. Math. Soc.* **51**, 555-562, (1945).

[39] S.M. Wise, J.S. Lowengrub, J.S. Kim, and W.C. Johnson, Efficient phase-field simulation of quantum dot formation in a strained heteroepitaxial film, *Superlattices and Microstructures* **36**, 293-304 (2004).

[40] S.M. Wise, J.S. Lowengrub, J.S. Kim, K. Thornton, P.W. Voorhees, and W.C. Johnson, Quantum dot formation on a strain-patterned epitaxial thin film, *App. Phys. Lett.* **87**, Art. No. 133102 (2005).